Supplementary information

Introducing a conductive pillar: a polyaniline intercalated layered titanate for high-rate and ultra-stable sodium and potassium ions storage

Jiaying Liao,[a] Qiao Hu,[a] Jinxiao Mu,[ab] Fei Chen,[a] Xiaodong He,[a] Fang Chen,[a] Zhaoyin Wen[b] and Chunhua Chen*[a]

[a] *CAS Key Laboratory of Materials for Energy Conversions, Department of Materials Science and Engineering & Collaborative Innovation Center of Suzhou Nano Science and Technology, University of Science and Technology of China, Hefei 230026, Anhui, China*

[b] *Shanghai Institute of Ceramics, Chinese Academy of Sciences, Shanghai 200050, China*

Experimental section

Materials synthesis

$Cs_{0.6}Ti_{1.85}\square_{0.15}O_4$ (CTO): The synthesis of CTO was carried out using a typical sol-gel method. 50 mmol $Ti(OC_4H_9)_4$ was dissolved in 50 ml of 5 M HNO_3, then 100 mmol citric acid and 10 mmol Cs_2CO_3 were added into the solution, respectively. The pH of the solution was adjusted to ~5.0 by concentrated $NH_3 \cdot H_2O$. Then the solution was transferred into a 1000 ml beaker and heated in an electric oven at 180 °C for 6 h to obtain a black sponge-like solid. Finally, the sponge-like solid was pre-calcined at 500 °C for 6 h and then sintered at 800 °C for 20 h in air.

HTO: It was obtained via the ion exchange reaction of CTO with 1M HCl (1 g CTO/100 mL HCl). The mixture of CTO and HCl was stirred for 24 h and washed thoroughly with deionized water. This step was repeated to exchange more Cs^+ ions with protons.

HTO-ANI: The intercalation of aniline in HTO was carried out following Scully et al.'s opration.[S1] 1 g of the as-obtained HTO was added to a mixture of 10 ml aniline and 10 ml deionized water. The intercalation of aniline was achieved by sonication of the mixture for 4 h, after which a homogeneous suspension was obtained. The aniline-intercalated product was recovered by centrifugation, washed thoroughly with ethanol for three times and then vacuum dried at 80 °C.

HTO-PANI: The intercalated aniline of HTO-ANI was polymerized by heat treatment at 140 °C for 12 h in an electric oven, the as-obtained product was marked as HTO-PANI-140. HTO-PANI-140 was further sintered at 400, 600 and 800 °C for 2 h in N_2, respectively, and the final products were marked as HTO-PANI-400, -600, and -800.

Characterization

The phases of as-obtained titanates were characterized with an X-ray diffractometer (Rigaku TTR-III, Cu Kα radiation). The morphology of the samples was studied with scanning electron microscopy (SEM, FEI Apreo) and transmission electron microscopy (TEM, JEM-2100F). The elemental mappings were analyzed by energy dispersive X-ray spectroscopy (EDS) attached to the SEM instrument. Thermogravimetric analysis (TGA) was performed at a heating rate of 10 °C min^{-1} in the temperature range of 25-800 °C under flowing air and N_2 atmosphere, respectively (DTG-60H, Shinadzu). Raman spectra were recorded on the condition of 532 nm diode laser excitation (Renishaw inVia Raman Microscope). The element information and valence states of elements were also determined by X-ray photoelectron spectroscopy (XPS, Escalab 250).

Electrochemical evaluation

The electrodes were prepared by mixing the active materials (70 wt. %), acetylene black (20 wt. %) and carboxymethyl cellulose binder (10 wt. %) in deionized water to obtain slurries, which were coated on a copper foil collector and vacuum dried at 80 °C. The typical mass loading was about 1.5 mg cm^{-2}. The electrochemical properties of the obtained materials were evaluated in coin-type cells (CR2032 size), which were assembled in an argon filled glove box (O_2 and H_2O < 0.1 ppm). For the fabrication of sodium half cells, sodium metal was used as the counter electrode, 1 M $NaClO_4$ in

ethylene carbonate (EC)/diethyl carbonate (DEC) (1:1 by volume, with 5% fluoroethylene carbonate additive) was used as the electrolyte. For the fabrication of potassium half cells, potassium metal was used as the counter electrode, 3 M potassium bis(fluorosulfonyl)imide (KFSI) in 1, 2-dimethoxyethane (DME) was used as the electrolyte. And a Whatman glass-fiber separator was used for each cell. The cyclic voltammetry (CV) of the cells was conducted on a CHI 660e electrochemical workstation in a voltage range from 0.01 to 3.0 V at the scan rate of 0.1-5.0 mV s^{-1}. The electrochemical impedance spectra (EIS) were measured through a frequency range between 0.01 Hz to 100 kHz. The cells were also galvanostatically cycled on a multi-channel battery test system (Neware BTS-2300, Shenzhen) in the voltage range from 0.01 to 3.0 V.
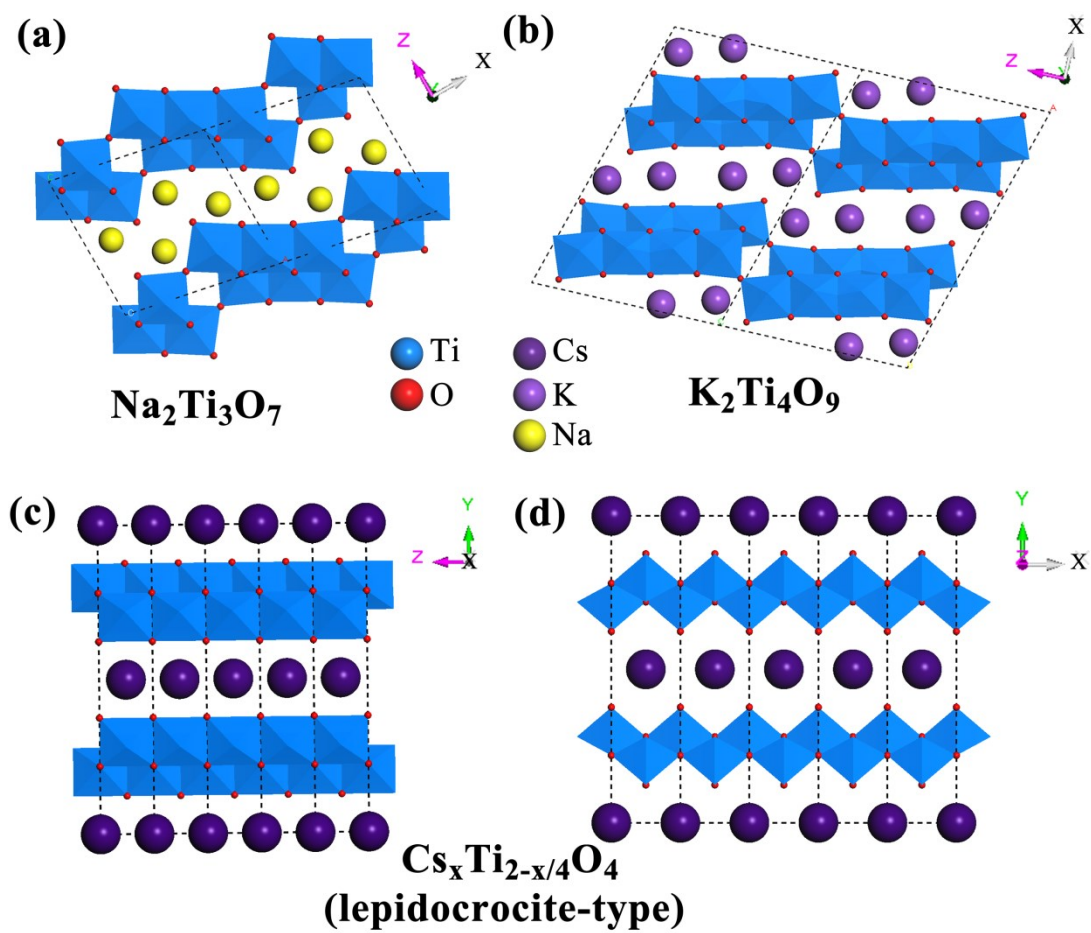
Fig. S1. Crystal structures of $Na_2Ti_3O_7$ (a), $K_2Ti_4O_9$ (b), and lepidocrocite-type $Cs_xTi_{2-4/x}O_4$ view from [100] (c) and [001] (d) directions.
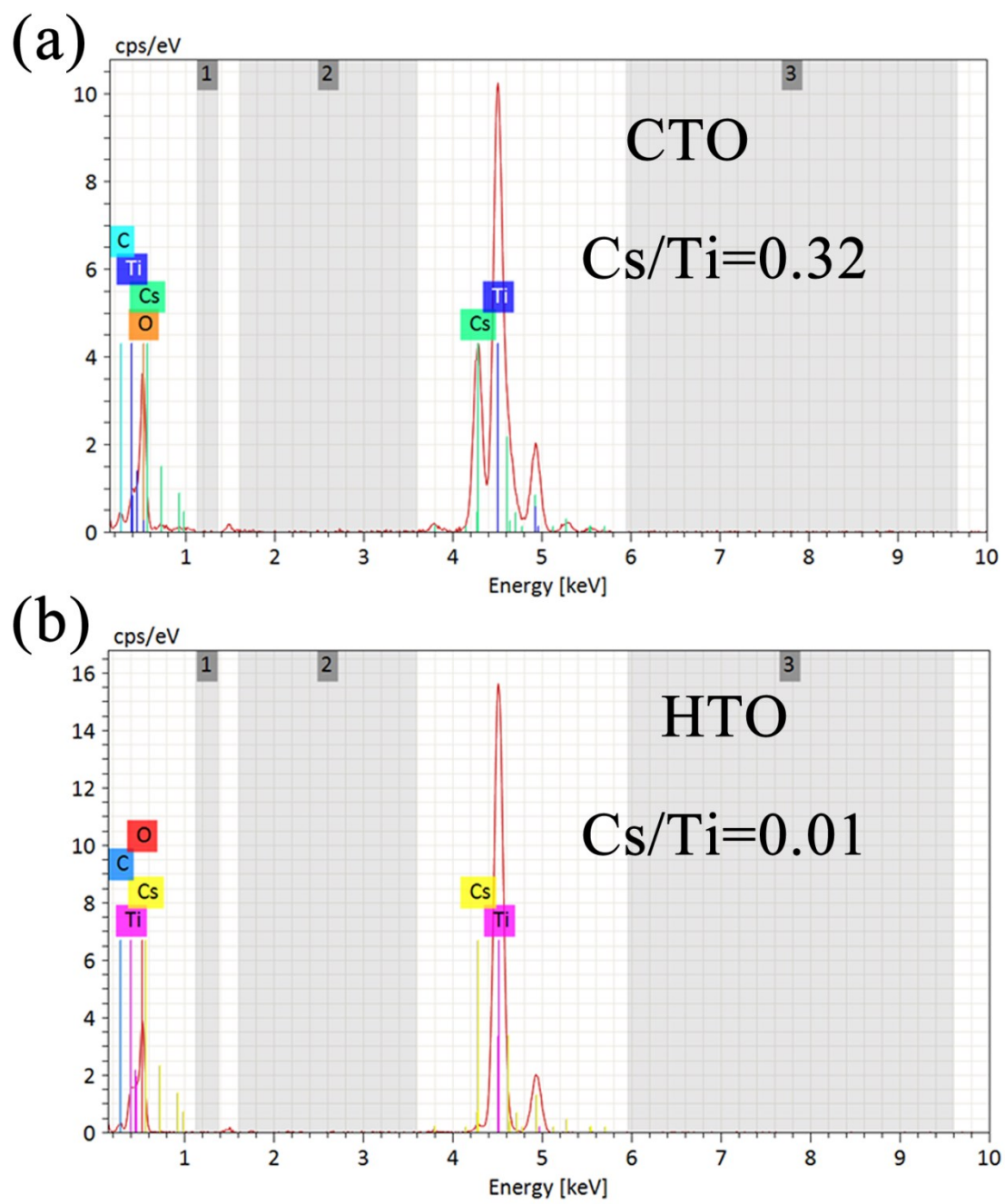
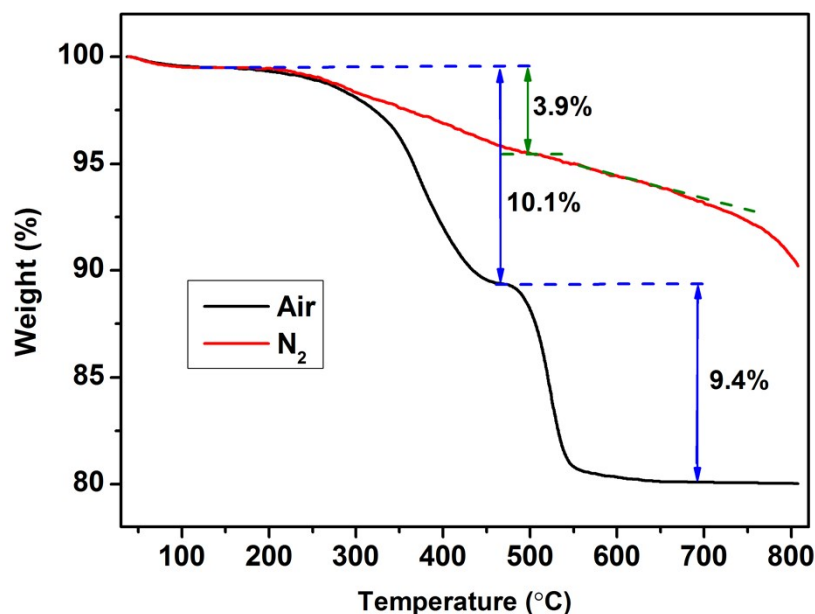**Fig. S2.** EDS results of CTO (a) and HTO (b).

Fig. S3. TG curves of HTO-PANI-140 measured in air and N_2.

Thermogravimetric (TG) analysis was carried out to measure the thermal stability and composition of HTO-PANI-140. The TG curve measured in air shows two distinct mass loss regions. The first mass loss (200-450 °C) is assigned to the combination of HTO dehydration and carbonization of polyaniline. The second mass loss (470-540 °C) is attributed to burning-out of the carbon. For comparison, the TG curve measured in N_2 shows a long sloping mass loss.

To calculate the PNAI and H_2O contents in HTO-PANI-140, we assume the formula is $(C_6H_4NH)_xH_{0.6}Ti_{1.85}O_4 \cdot yH_2O$. The total weight loss (10.1% + 9.4%) in air is complete decomposition of HTO-PANI-140 to TiO_2, and the second weight loss region (470-540 °C, 9.4%) can be approximately attributed to burning-out of the carbon. Thus, we can calculate the x and y value are 0.25 and 0.4, respectively. Moreover, the total weight loss in N_2 (<500 °C, 3.9%) can be approximately attributed to H_2O, and the result is in accord with previous calculation ($0.4H_2O$).
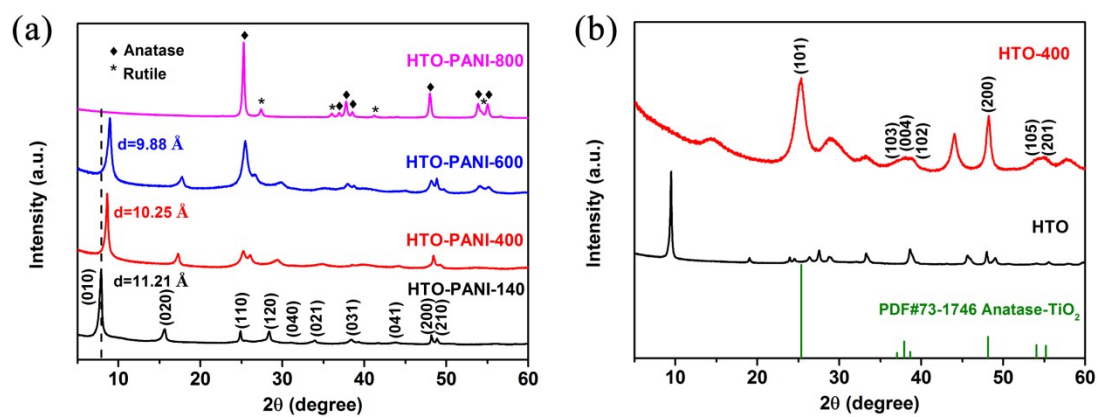
Fig. S4. XRD patterns of HTO-PANI after heat treatment at different temperatures (a), and HTO before and after heat treatment at 400 °C for 2h in N_2 (b).
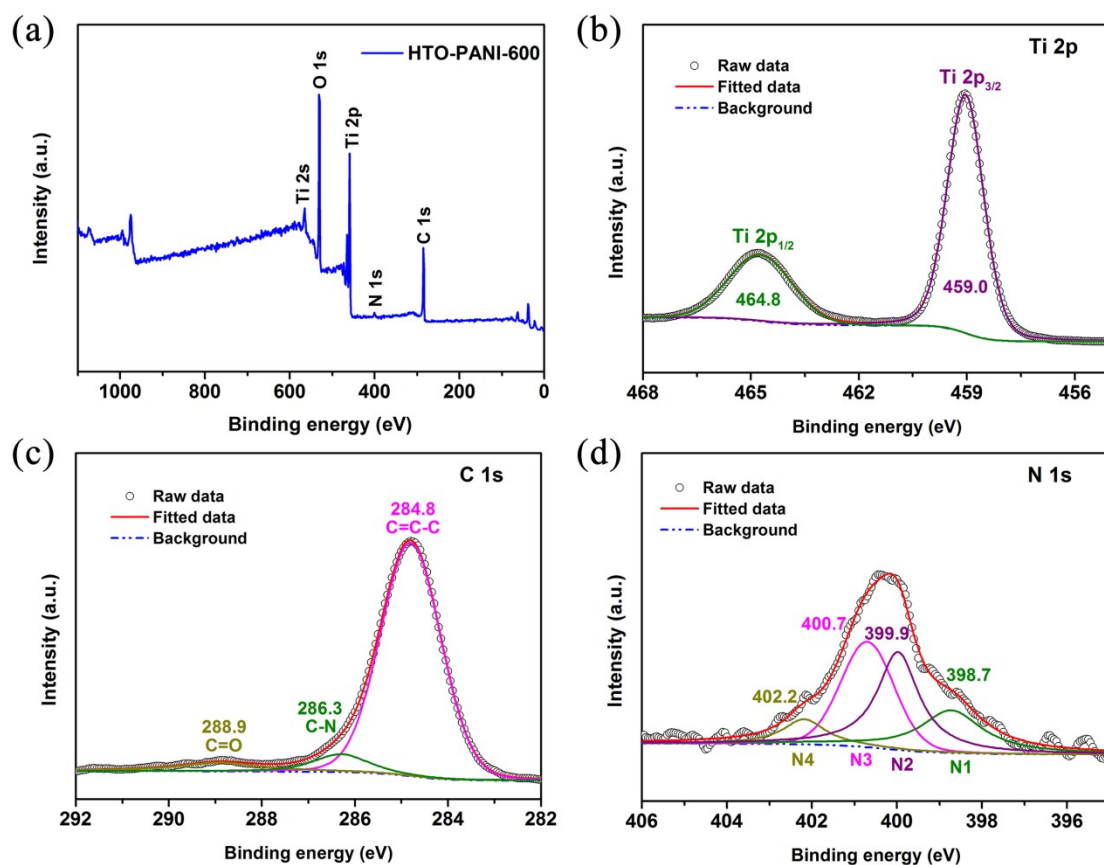

Fig. S5. XPS spectra of HTO-PANI-600: (a) full pattern; High-resolution XPS spectra of (b) Ti 2p, (c) C 1s, and (d) N 1s.
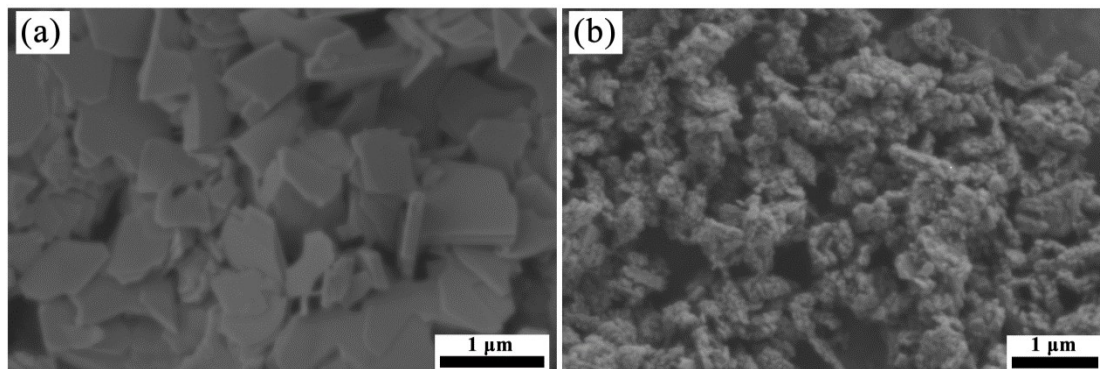
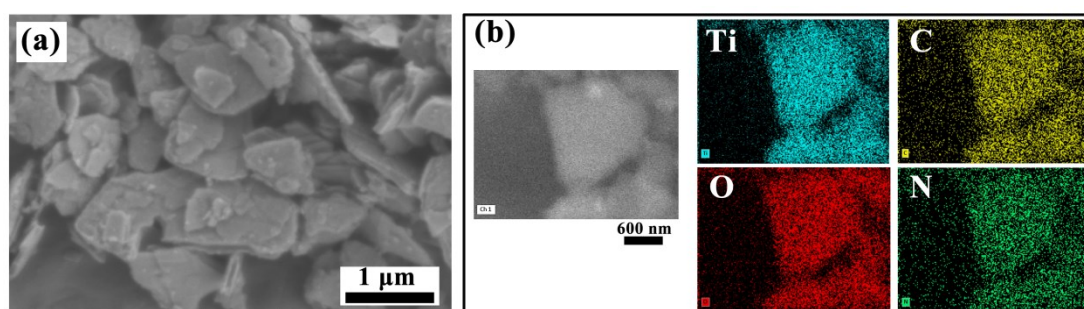**Fig. S6.** SEM images of CTO (a) and HTO-PANI-800 (b).

Fig. S7. (a) SEM image of the HTO-PANI-600; (b) SEM elemental mapping images of Ti, O, C, and N.
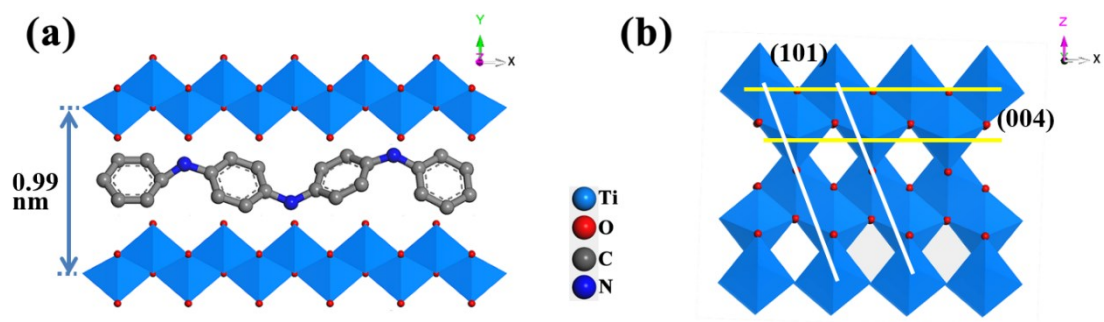

Fig.S8. Schematic illustration of dehydrated HTO-PANI (a) and anatase TiO_2 (b).
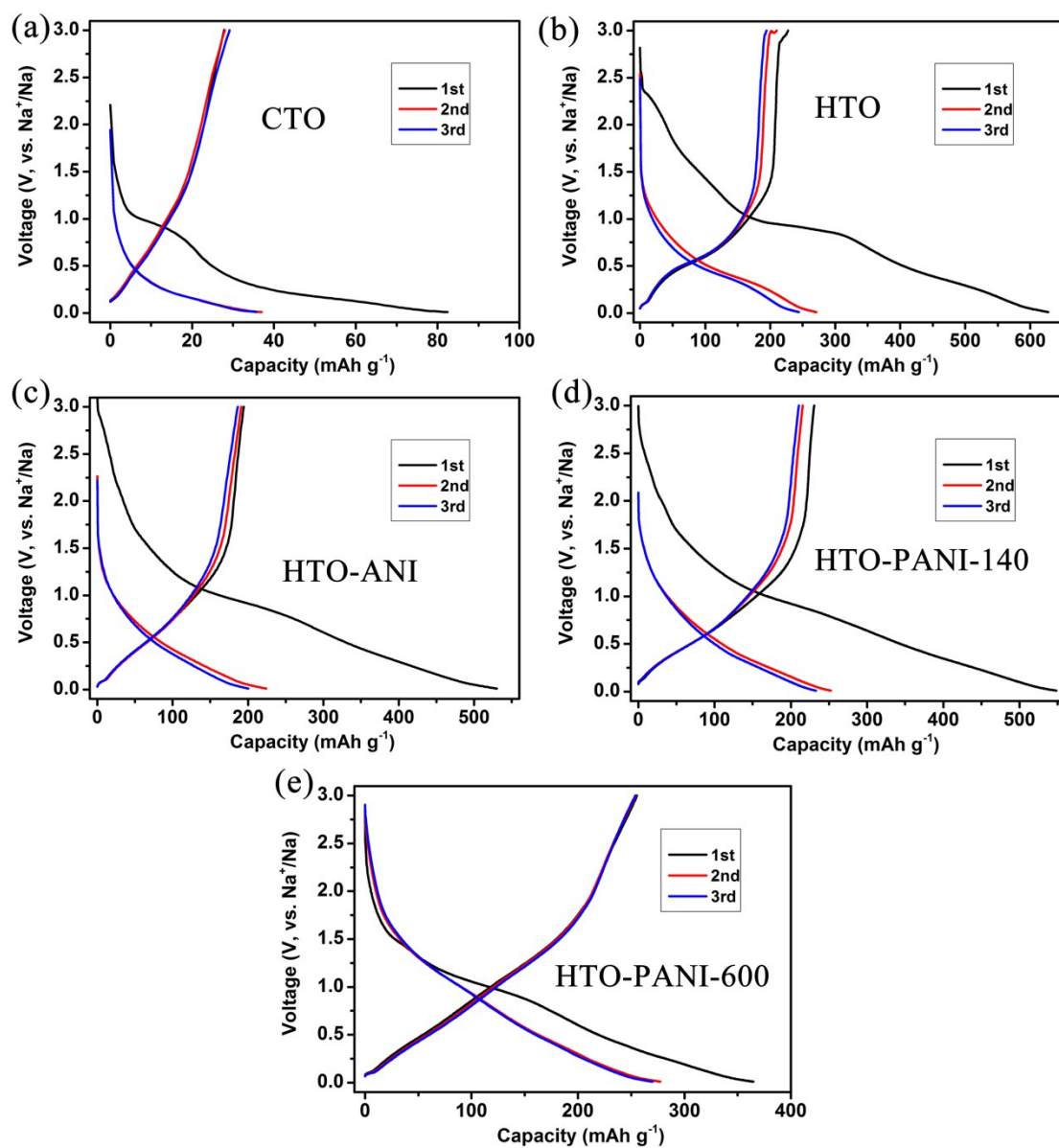
Fig. S9. Charge/discharge curves of the initial three cycles of the as-synthesized titanates at a current density of 50 mA g^{-1} in NIBs: (a) CTO; (b) HTO; (c) HTO-ANI; (d) HTO-PANI-140; (e) HTO-PANI-600.
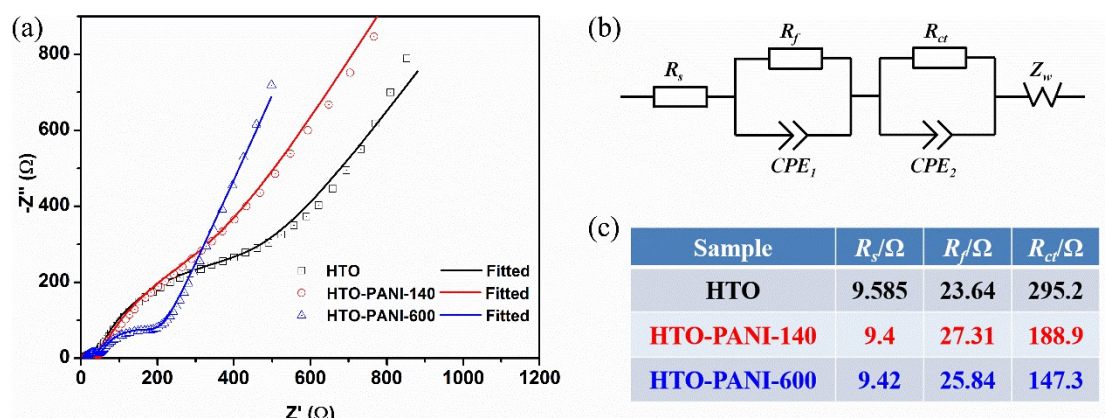
Fig. S10. (a) EIS spectra of HTO, HTO-PANI-140 and HTO-PANI-600; (b) the equivalent circuit used for simulating the experimental impedance data and (c) the fitted impedances. The cells were activated for three cycles in NIBs.

All of the EIS spectra consist of two semicircles in the high and middle frequency regions, and a sloping straight line in the low frequency region. The EIS spectra are fitted using the equivalent circuit model (Fig. S10b), where R_s represents solution resistance corresponding to the electrolyte and electrical contacts, R_f represents K^+ transfer resistance through the passivation film, and R_{ct} represents charge-transfer resistance for the electrons and K^+ ions. As can be seen for all of the samples, both R_s and R_f are approximately close to each other, while HTO-PANI-140 and HTO-PANI-600 deliver the lower R_{ct} values than HTO, corresponding to faster electrons and K^+ transport.
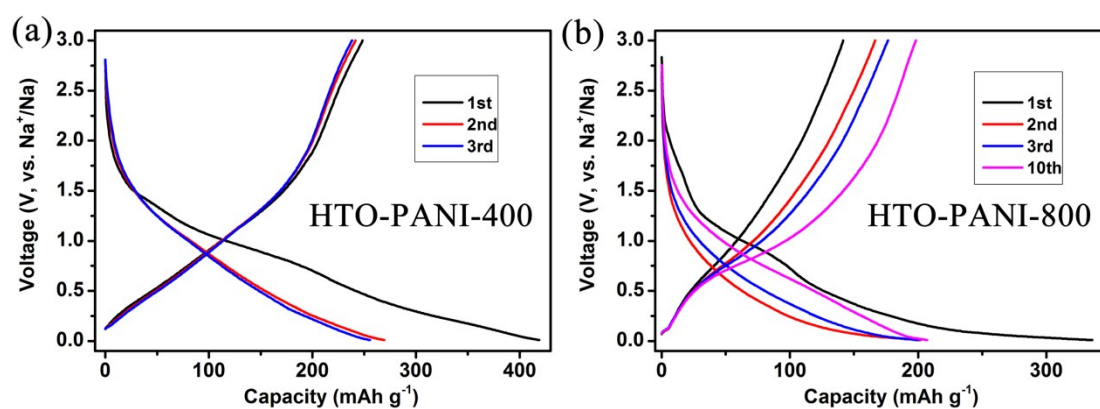

Fig. S11. Charge/discharge curves of the selected cycles of HTO-PANI-400 (a) and HTO-PANI-400 (b) at a current density of 50 mA g^{-1} in NIBs.
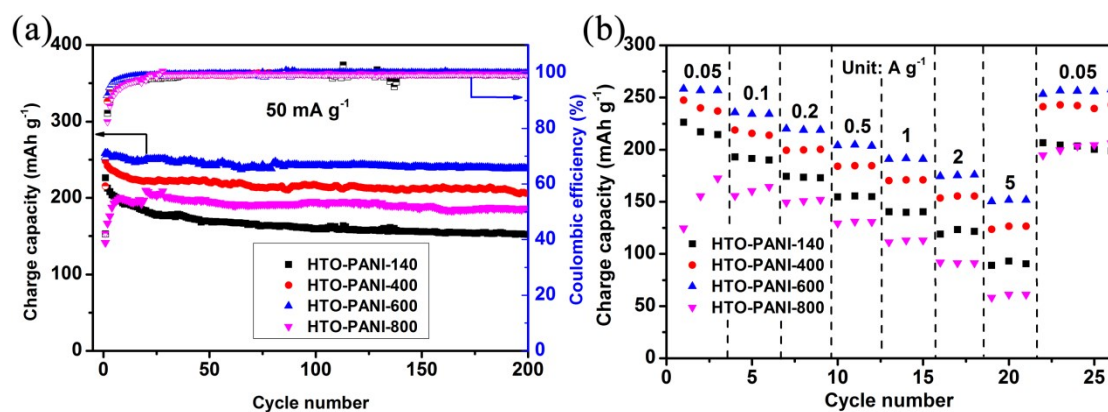
Fig. S12. Comparison of (a) cycling performance of the HTO-PANI after heat treatment at different temperatures at a current density of 50 mA g^{-1} and (b) rate performance from 0.05 to 5 A g^{-1} in NIBs.

Table S1. Comparison of the electrochemical performance of the as-synthesized materials in NIBs.

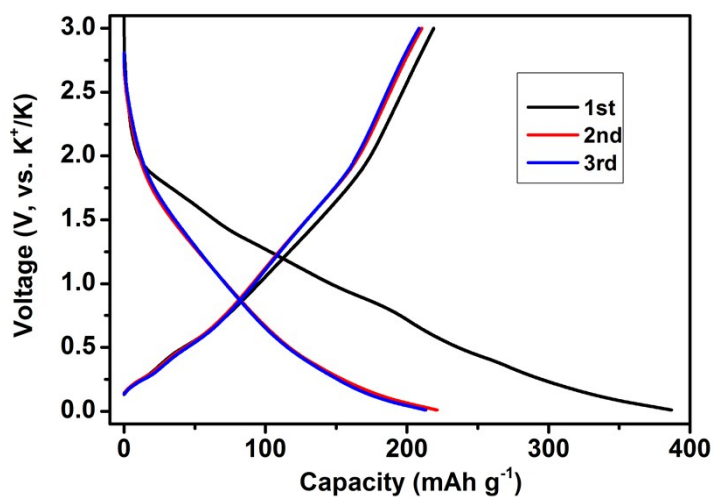| Composition	Capacity (mAh g^{-1})	Initial Coulombic efficiency	Capacity retention (200 cycles; @50 mA g^{-1})	Rate capability (@5A g^{-1})
CTO	38	33.9%	92.1%	~0
HTO	227	36.2%	38.3%	~0
HTO-ANI	194	36.6%	~0	15.5%
HTO-PANI-140	226	42.0%	67.3%	39.8%
HTO-PANI-400	248	59.3%	83.1%	50.8%
HTO-PANI-600	258	69.7%	92.3%	58.9%
HTO-PANI-800	208	42.2%	89.4%	29.3%

Fig. S13. Charge/discharge curves of the initial three cycles of HTO-PANI-600 at a current density of 50 mA g^{-1} in KIBs.
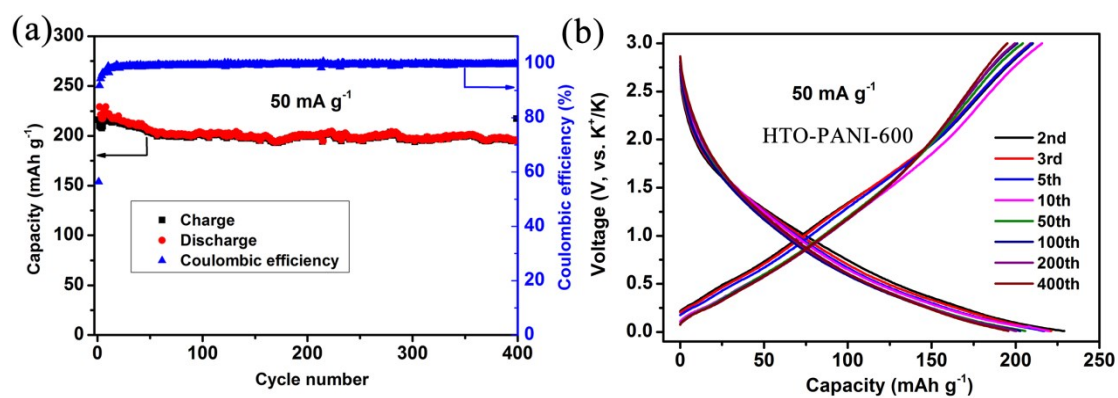
Fig. S14. (a) Cycling performance and (b) the charge/discharge curves of the selected cycles of HTO-PANI-600 at a current density of 50 mA g^{-1} in KIBs.
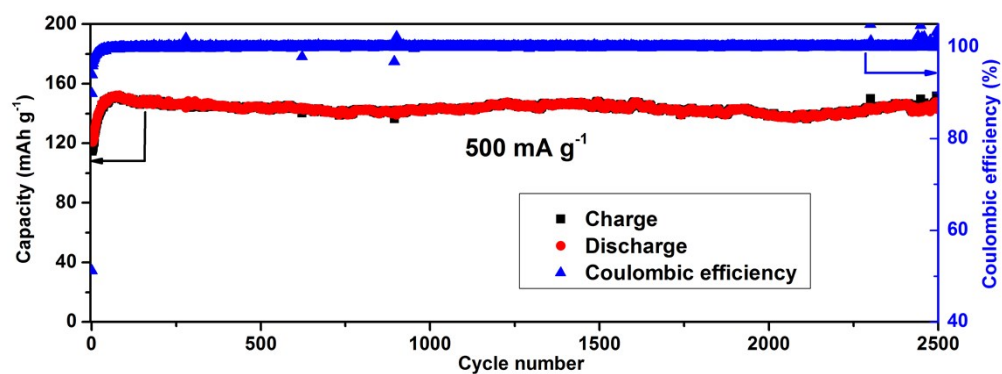
Fig. S15. Long-life cycling of HTO-PANI-600 at a current density of 500 mA g^{-1} in KIBs.
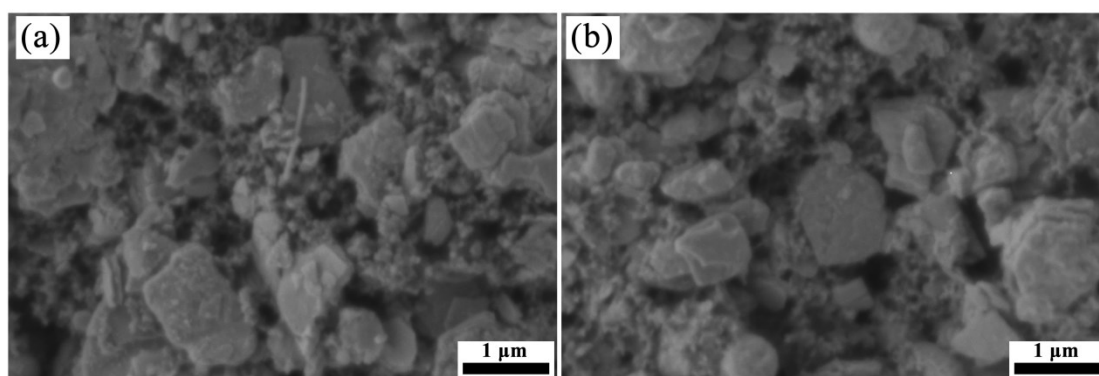
Fig. S16. SEM images of HTO-PANI-600 electrodes after cycling in NIBs (a) and KIBs (b).
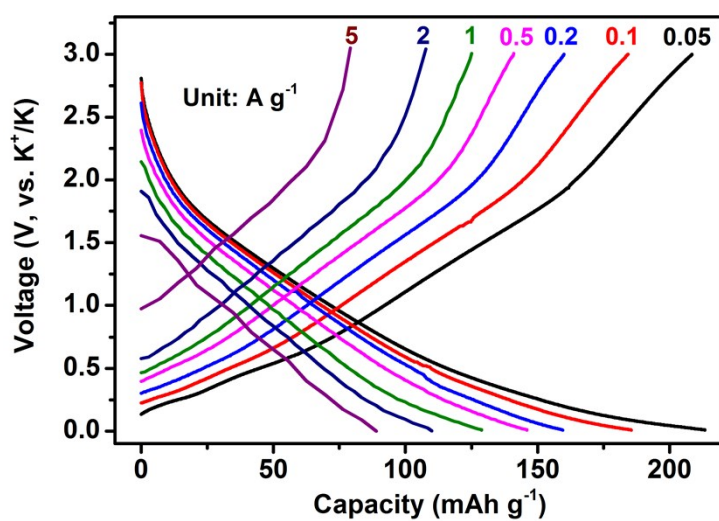
Fig. S17. Discharge/charge curves of HTO-PANI-600 at different current densities in KIBs.
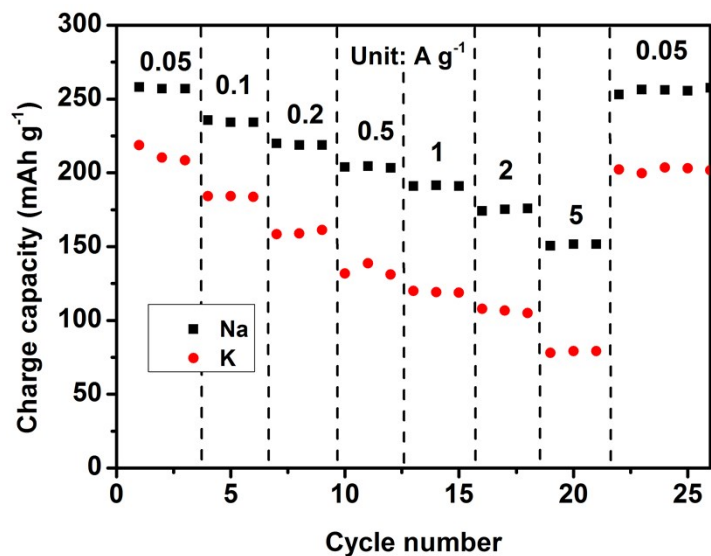
Fig. S18. Comparison of the rate performance of the HTO-PANI-600 in NIBs and KIBs.
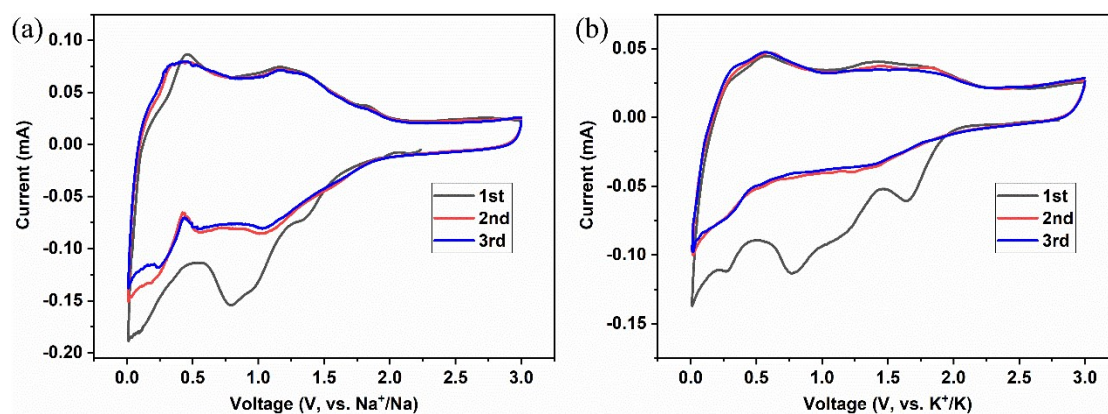
Fig. S19. Initial three cycles of CV curves of HTO-PANI-600 in NIBs (a) and KIBs (b) at a scan rate of 0.1 mV s^{-1}.

The first cycle of CV curves is quite different from the others, owing to some irreversible reactions and the formation of SEI. The second and third cycles are nearly overlapped in both of NIBs and KIBs, indicating the good electrochemical reversibility.

Fig. S20. CV curves of HTO-PANI-600 at various sweep rates from 0.1 to 5.0 mV s^{-1} in NIBs (a) and KIBs (d); Separation of the capacitive and diffusion-controlled currents at a sweep rate of 0.5 mV s^{-1} in NIBs (b) and KIBs (e); Contribution ratio of the capacitive and diffusion-controlled charge at various sweep rates in NIBs (c) and KIBs (f).

Cyclic voltammetry (CV) of the HTO-PANI-600 electrode is carried out to investigate the electrochemical kinetics of sodium and potassium storages in the layered ti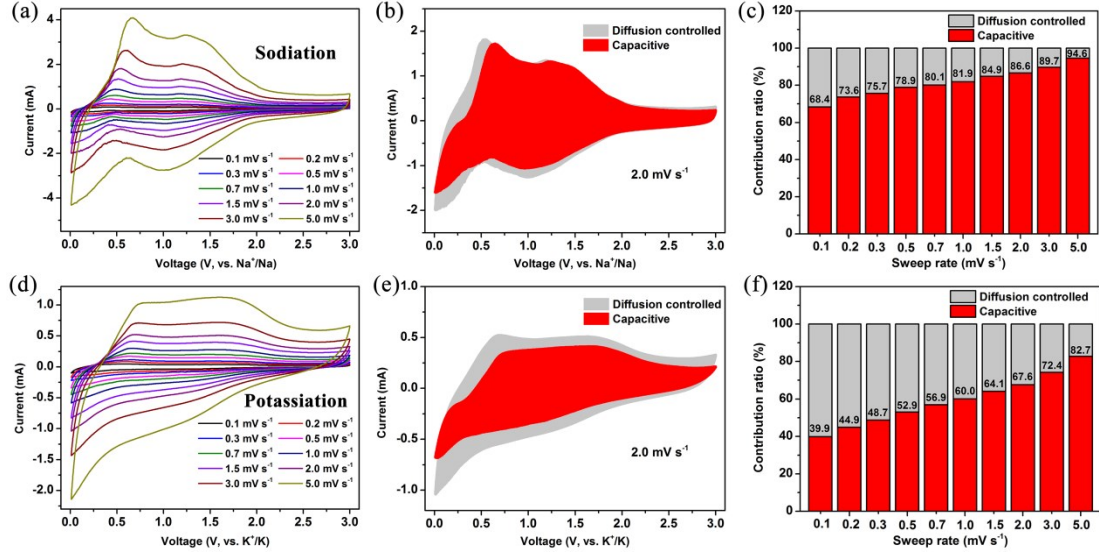tanate. We separate of the capacitive and diffusion-controlled currents from CV measurements according to Wang et al's work [S2]. The total capacitive contribution at a certain scan rate can be quantified by separating the specific contribution from the capacitive effects (k_1v) and diffusion-controlled process ($k_2v^{1/2}$) at a particular voltage according to following relationship:

$$i(\text{V}) = k_1v + k_2v^{1/2} \tag{1}$$

where k_1 and k_2 are constants at a certain sweep rate. Thus, by determining k_1 and k_2, we are able to quantify, at specific potentials, the fraction of the current due to each of these contributions.

For analytical purposes, we rearrange eq (1) slightly to

$$i(\text{V})/v^{1/2} = k_1v^{1/2} + k_2 \tag{2}$$

The k_1 and k_2-value can be determined by the slope and intercept of the $v^{1/2}$ against $i(V)/v^{1/2}$ plots, respectively. Then, we draw the curve of $i_c(V) = k_1 v$, and the area of the curve is capacitive contribution at a certain scan rate.

The capacitive charge contributes to 68.4% of the total capacity even at a low sweep rate of 0.1 mV s^{-1} in NIBs. Lower capacitive charge contributions are observed in KIBs, in accord with its relatively sluggish kinetics.
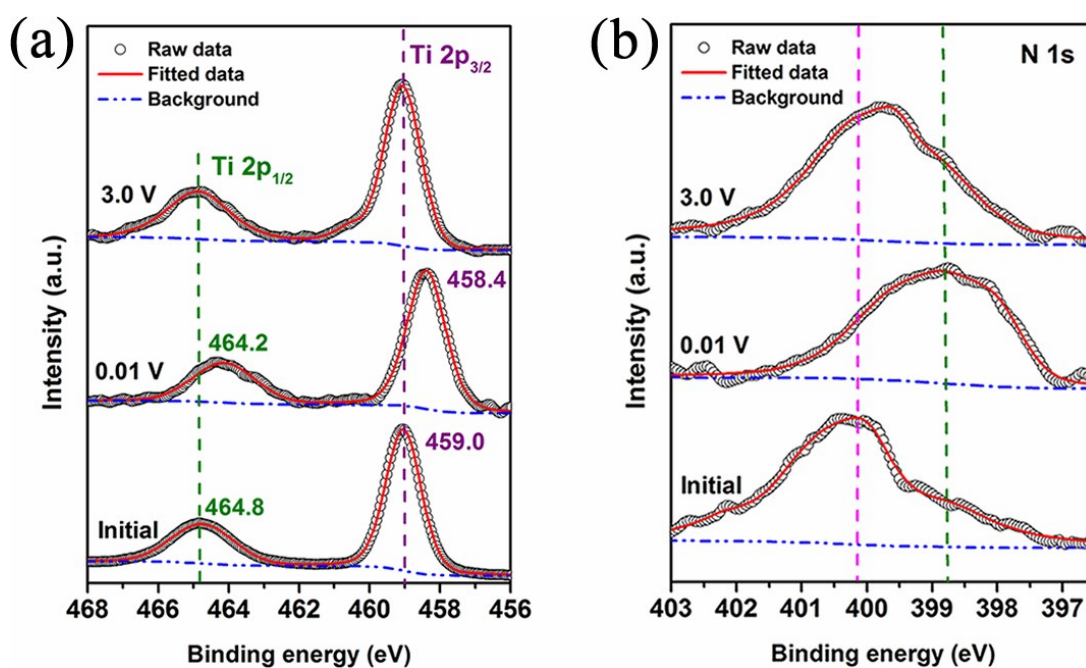
Fig. S21. High-resolution XPS spectra of Ti 2p (a) and N 1s (b) at different electrochemical stages in KIBs.
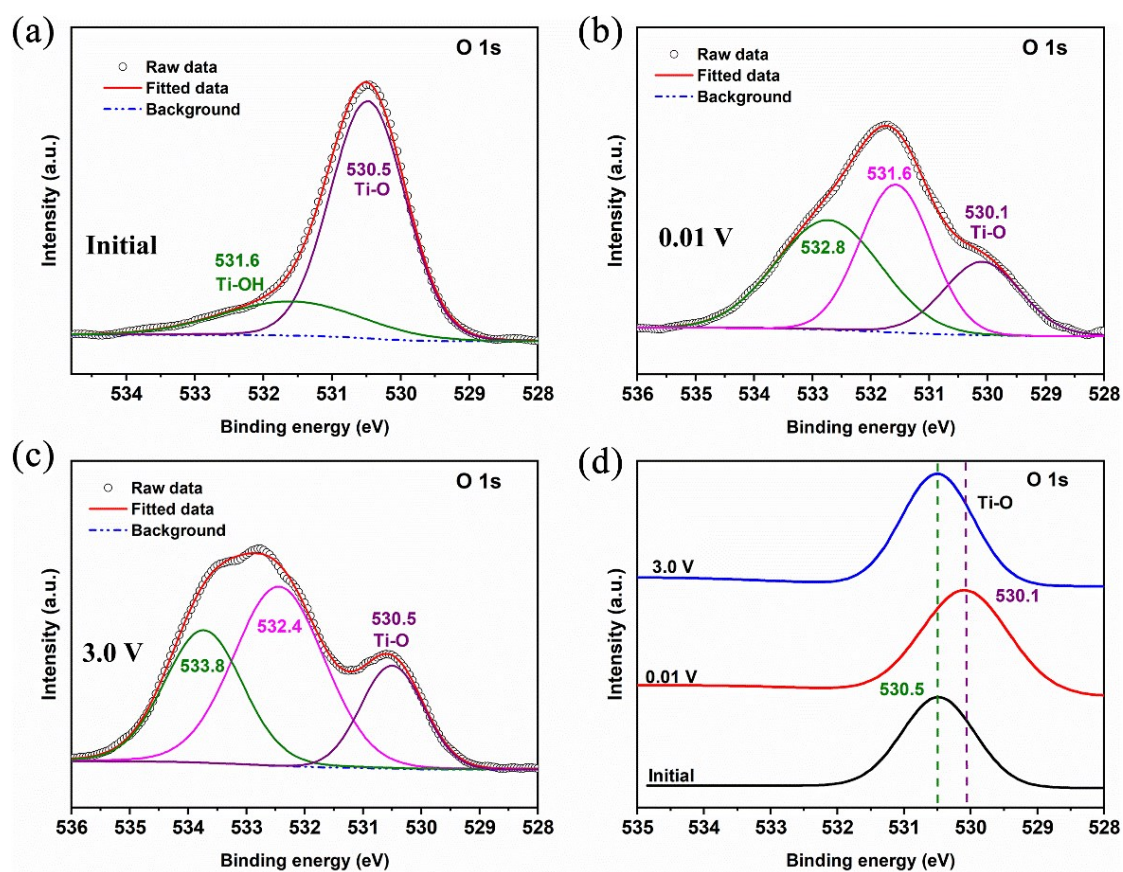
Fig. S22. (a-c) High-resolution XPS spectra of O 1s at different electrochemical stages in KIBs; (d) Comparison of the binding energy of Ti-O at different electrochemical stages.

The peaks centered at about 530 eV are attributed to Ti-O binding, and the peaks centered at higher binding energy are attributed to oxyhydroxide and the oxide in SEI. In Fig. S22d, we find that the binding energy of Ti-O decreases during the potassiation and then shifts back upon the depotassiation.

Table S2. Comparison of the electrochemical performances of the titanate-based materials in NIBs.

Composition	Initial Coulombic efficiency	Reversible capacity $(mAh\ g^{-1})$	Cycling stability	References
$K_{0.8}Ti_{1.73}Li_{0.27}O_4@C$	28.3%	**119.6** (20 mA g^{-1}) **66** (200 mA g^{-1})	115.1% after 250 cycles at 20 mA g^{-1}	[S3]
$Na_{0.9}Ti_{1.7}Li_{0.3}O_4$ $\cdot nH_2O$	38% (PVDF)	**100** (10 mA g^{-1})	70% after 100 cycles at 10 mA g^{-1}	[S4]
$Na_{0.9}Ti_{1.7}Li_{0.3}O_4$	57% (PVDF) 76% (PAN)	**120** (10 mA g^{-1})	75% after 100 cycles at 10 mA g^{-1}	[S5]
$K_2Ti_8O_{17}@Ti_3SiC_2$	38%, 88% (presodiation)	**210** (200 mA g^{-1}) **118** (6 A g^{-1})	91.0% after 200 cycles at 200 mA g^{-1}	[S6]
$NaTi_{1.5}O_{8.3}$ from Ti_3C_2	51%	**196** (50 mA g^{-1}) **101** (2 A g^{-1})	73% after 150 cycles at 200 mA g^{-1}	[S6]
$Na_2Ti_3O_7@RGO$ from $Ti_3C_2T_x$	26%	**302** (100 mA g^{-1}) **97** (5 A g^{-1})	55% after 10000 cycles at 5 A g^{-1}	[S7]
$Mg_{0.2}H_{0.64}(Ti_{1.74}O_4)_{1.04}$ $\cdot1.5H_2O$	56%	**188** (50 mA g^{-1}) **110** (3 A g^{-1})	80.6% after 10000 cycles at 3 A g^{-1}	[S8]
$TiO_2@Graphene$	50.6%	**202** (83 mA g^{-1}) **59.8** (4.187 A g^{-1})	94.4% after 4000 cycles at 3.35 A g^{-1}	[S9]
HTO-PANI-600	69.7%	**258** (50 mA g^{-1}) **151** (5 A g^{-1})	92.3% after 200 cycles at 50 mA g^{-1}; 99.6% after 2500 cycles at 1 A g^{-1}	This work

Table S3. Comparison of the electrochemical performances of the titanate-based materials in KIBs.

Composition	Initial Coulombic efficiency	Reversible capacity (mAh g^{-1})	Cycling stability	References
$K_2Ti_4O_9$	20%	**97** (30 mA g^{-1}) **20** (2 A g^{-1})	56% after 30 cycles at 100 mA g^{-1}	[S10]
$K_2Ti_6O_{13}$	27.8%	**150** (28 mA g^{-1}) **20** (1.4 A g^{-1})	73% after 200 cycles at 28 mA g^{-1}	[S11]
$K_2Ti_8O_{17}$	63.6%	**120** (20 mA g^{-1}) **44** (500 mA g^{-1})	85% after 50 cycles at 20 mA g^{-1}	[S12]
$K_2Ti_4O_9$ from Ti_3C_2	25.9%	**151** (50 mA g^{-1}) **81** (300 mA g^{-1})	51% after 900 cycles at 200 mA g^{-1}	[S6]
Ti_3CNT_z	28.4%	**202** (20 mA g^{-1}) **32** (500 mA g^{-1})	37.1% after 100 cycles at 20 mA g^{-1}	[S13]
$K_2Ti_4O_9$@RGO from $Ti_3C_2T_x$	24%	**218** (100 mA g^{-1}) **75** (2 A g^{-1})	88% after 700 cycles at 2 A g^{-1}	[S7]
$Mg_{0.2}H_{0.64}(Ti_{1.74}O_4)_{1.04}$ $\cdot 1.5H_2O$	48%	**177** (50 mA g^{-1}) **87** (3 A g^{-1})	70% after 1000 cycles at 1 A g^{-1}	[S8]
TiO_2 hierarchical tubular	49.1%	**240.8** (100 mA g^{-1}) **97.3** (2 A g^{-1})	81.3% after 1200 cycles at 500 mA g^{-1}	[S14]
HTO-PANI-600	56.6%	**219** (50 mA g^{-1}) **81** (5 A g^{-1})	90.5% after 400 cycles at 50 mA g^{-1}; 97.2% after 2500 cycles at 500 mA g^{-1}	This work

References

[S1] S. F. Scully, R. Bissessur, *Synthetic Met.* 2009, **159**, 637-641.

[S2] J. Wang, J. Polleux, J. Lim and B. Dunn, *J. Phys. Chem. C*, 2007, **111**, 14925-14931

[S3] K. Y. Chen, W. X. Zhang, Y. Liu, H. P. Zhu, J. Duan, X. H. Xiang, L. H. Xue, Y. H. Huang, *Chem. Commun.* 2015, **51**, 1608-1611.

[S4] A. Katogi, K. Kubota, K. Chihara, K. Miyamoto, T. Hasegawa, S. Komaba, *ACS Appl. Energy Mater.* 2018, **1**, 3630-3635.

[S5] G. Zou, J. Guo, X. Liu, Q. Zhang, G. Huang, C. Fernandez, Q. Peng, *Adv. Energy Mater.* 2017, **7**, 1700700.

[S6] C. Zeng, F. Xie, X. Yang, M. Jaroniec, L. Zhang, S.-Z. Qiao, *Angew. Chem.* 2018, **57**, 8540-8544.

[S7] Y. Dong, Z.-S. Wu, S. Zheng, X. Wang, J. Qin, S. Wang, X. Shi, X. Bao, *ACS Nano* 2017, **11**, 4792-4800.

[S8] J. Yang, X. Xiao, W. Gong, L. Zhao, G. Li, K. Jiang, R. Ma, M. H. Rummeli, F. Li, T. Sasaki, F. Geng, *Angew. Chem.* 2019, **58**, 8740-8745.

[S9] Y. Zhang, C. W. Foster, C. E. Banks, L. Shao, H. Hou, G. Zou, J. Chen, Z. Huang, X. Ji, *Adv. Mater.* 2016, **28**, 9391-9399.

[S10] B. Kishore, V. G, N. Munichandraiah, *J. Electrochem. Soc.* 2016, **163**, A2551-A2554.

[S11] S.-M. Xu, Y.-C. Ding, X. Liu, Q. Zhang, K.-X. Wang, J.-S. Chen, *Adv. Energy Mater.* 2018, **8**, 1802175.

[S12] J. Han, M. Xu, Y. Niu, G. N. Li, M. Wang, Y. Zhang, M. Jia, C. M. Li, *Chem. Commun.* 2016, **52**, 11274-11276.

[S13] M. Naguib, R. A. Adams, Y. Zhao, D. Zemlyanov, A. Varma, J. Nanda, V. G. Pol, *Chem. Commun.* 2017, **53**, 6883-6886.

[S14] Y. Li, C. Yang, F. Zheng, Q. Pan, Y. Liu, G. Wang, T. Liu, J. Hu, M. Liu, *Nano Energy* 2019, **59**, 582-590.